

Interpretation of the propagation of surface altimetric observations in terms of planetary waves and geostrophic turbulence

Ross Tulloch,¹ John Marshall,² and K. Shafer Smith¹

Received 29 July 2008; revised 5 November 2008; accepted 11 December 2008; published 12 February 2009.

[1] The interpretation of surface altimetric signals in terms of Rossby waves is revisited. Rather than make the long-wave approximation, the horizontal scale of the waves is adjusted to optimally fit the phase speed predicted by linear theory to that observed by altimetry, assuming a first baroclinic mode vertical structure. It is found that in the tropical band the observations can be fit if the wavelength of the waves is assumed to be large, of order 600 km or so. However poleward of $\pm 30^\circ$, it is more difficult to fit linear theory to the observations, and the fit is less good than at lower latitudes: the required scale of the waves must be reduced to about 100 km, somewhat larger than the local deformation wavelength. It is argued that these results can be interpreted in terms of Rossby wave, baroclinic instability, and turbulence theory. At low latitudes there is an overlap between geostrophic turbulence and Rossby wave timescales, and so, an upscale energy transfer from baroclinic instability at the deformation scale produces waves. At high latitudes there is no such overlap and waves are not produced by upscale energy transfer. These ideas are tested by using surface drifter data to infer turbulent velocities and timescales that are compared to those of linear Rossby waves. A transition from a field dominated by waves to one dominated by turbulence occurs at about $\pm 30^\circ$, broadly consistent with the transition that is required to fit linear theory to altimetric observations.

Citation: Tulloch, R., J. Marshall, and K. S. Smith (2009), Interpretation of the propagation of surface altimetric observations in terms of planetary waves and geostrophic turbulence, *J. Geophys. Res.*, 114, C02005, doi:10.1029/2008JC005055.

1. Introduction

[2] Altimetric observations of sea surface height (SSH) of the ocean show westward propagating phase anomalies in all of the major oceans except the Antarctic Circumpolar Current (ACC), the Kuroshio and the Gulf Stream, where the propagation is eastward. *Chelton and Schlax* [1996] attempted to understand these observations in terms of linear, first baroclinic Rossby waves in a resting ocean and in the long-wave limit. They found that observed phase speeds were larger than predicted by theory outside the tropics by as much as a factor of two (see, e.g., the introduction of *Colin de Verdière and Tailleux* [2005], who review an extensive literature on the subject). *Chelton et al.* [2007] recently observed that SSH variability appears to be nondispersive and consistent with the behavior of nonlinear eddies in many regions of the world ocean, particularly poleward of 25° , in western basins and in the ACC. Some of the discrepancy between the observations and linear theory can be resolved by including mean flow and topography [*Killworth et al.*, 1997; *Dewar and Morris*, 2000;

Killworth and Blundell, 2005; *Maharaj et al.*, 2007]. We find that the “fit” of linear theory to observations at high latitudes is not as successful as at low latitudes. However, the downstream phase speed observed in the ACC is captured rather well. Less satisfying, is the mismatch of best fit speeds to observations in the 40° to 50° latitude bands. *Killworth and Blundell* [2005] appear to obtain a closer fit there, the reasons for which are not clear to us.

[3] A number of authors adopt the planetary geostrophic approximation [*Dewar*, 1998, appendix; *Killworth and Blundell*, 1999, 2003; *Colin de Verdière and Tailleux*, 2005] and so automatically make the long-wave approximation by neglecting relative vorticity. Others have considered Rossby basin modes in the quasi-geostrophic approximation [*Cessi and Primeau*, 2001; *LaCasce and Pedlosky*, 2004]. As noted by *Killworth and Blundell* [2005], all such calculations implicitly assume production of waves at the eastern boundary, yet their ray tracing calculations through the observed hydrography indicate that such waves are generally unable to cross the basin. Instead, *Killworth and Blundell* [2007] investigate the assumption that waves are produced throughout the ocean via local forcing by winds, buoyancy exchange or baroclinic instability of the mean state; they put this assumption to use by computing the dispersion relation at each lateral position, assuming local forcing and horizontal homogeneity (i.e., doubly periodic boundary conditions for each $1^\circ \times 1^\circ$ section, the “local approximation”).

¹Center for Atmosphere Ocean Science, Courant Institute of Mathematical Sciences, New York University, New York, USA.

²Department of Earth, Atmospheric and Planetary Sciences, Massachusetts Institute of Technology, Cambridge, Massachusetts, USA.

[4] Both *Killworth and Blundell* [2007] and *Smith* [2007] (in a similar analysis) find that the oceans are rife with baroclinic instability, occurring at or below the deformation scale, thus providing a ready source of energy, cascading upscale from below, for the waves and turbulence seen at the ocean's surface. Indeed both altimeter observations and numerical ocean models provide evidence of an inverse spectral flux of kinetic energy from the deformation scale up to an arrest wavelength of order 500–1000 km, which decreases with latitude but does not scale closely with the deformation scale [*Scott and Wang*, 2005; *Schlösser and Eden*, 2007]. Such an inverse cascade is possibly the result of nonlinear interactions in geostrophic turbulence. (The inverse cascade observed by *Scott and Wang* [2005] presented a conundrum since up to 70% of the variability at the ocean surface is contained in the first baroclinic mode [*Wunsch*, 1997], and it was thought that first baroclinic energy should cascade toward the Rossby radius. However *Scott and Arbic* [2007] showed in simulations of two-layer baroclinic turbulence, that while the total energy in the first baroclinic mode cascades toward the Rossby radius, the kinetic energy moves upscale.) The inverse cascade can be arrested or slowed before reaching the basin scale by Rossby waves [*Rhines*, 1975], stratification $N^2(z)$ (when energy is contained in baroclinic modes, particularly if N^2 is surface intensified as in the ocean [see *Fu and Flierl*, 1980; *Smith and Vallis*, 2001]), or dissipative processes [*Arbic and Flierl*, 2004; *Thompson and Young*, 2006]. It is not yet clear which of these processes, if any of them, sets the ultimate arrest scale.

[5] *Rhines* [1975] theorized that, because the eddy timescale increases as the spatial scale grows in the inverse cascade, a transition will occur at the spatial scale where the eddy timescale matches that of Rossby waves with the same spatial scale. The transition scale, commonly referred to as the Rhines scale, is $L_R \sim (2u_t/\beta)^{1/2}$, where u_t is the square root of the eddy kinetic energy (which, in the two-dimensional system considered, is the only energy). It is at this spatial scale, *Rhines* suggested, that the turbulent energy is shunted into either jets or waves, or both, depending on the strength and homogeneity of the eddy field. Numerical experiments presented by *Rhines* demonstrate that, even when the eddies are energetic enough to form jets, Rossby waves may also be energized. *Vallis and Maltrud* [1993] refined the idea of a wave-turbulence crossover by noting that while the Rhines effect cannot halt the cascade alone, it inhibits energy transfer into a dumbbell-shaped region around the origin in wave number space, which leads to the generation of zonally elongated flow. There is some evidence for zonal jet formation in the ocean [*Maximenko et al.*, 2005; *Richards et al.*, 2006], perhaps a signature of the Rhines effect, in addition to the observations of waves by *Chelton and Schlax* [1996] and *Chelton et al.* [2007].

[6] Recent research [*Theiss*, 2004; *Smith*, 2004] has suggested that, on the giant gas planets, turbulent generation at small scales should result in jet formation in regions equatorward of some critical latitude, and a more isotropic eddy field in regions poleward of that critical latitude. *Scott and Polvani* [2007] confirmed that a critical latitude for jet formation does arise in direct numerical simulations of forced dissipative shallow-water turbulence on the sphere. *Theiss* [2006] extends the idea further by replacing β with the mean flow-dependent meridional potential vorticity (PV). Spe-

cifically, he derives a “generalized” Rhines scale, which includes the effect of mean shears, and a corresponding critical latitude, poleward of which jets do not form.

[7] Following on these ideas, *Eden* [2007] analyzed eddy length scales in the North Atlantic Ocean both via satellite altimetry and an eddy resolving primitive equation model. At high latitudes, he shows evidence that eddy scales vary with the Rossby deformation radius, consistent with *Stammer* [1997], while at low latitudes, eddy scales are consistent with a generalized Rhines scale. That is, eddies scale with the smaller of the deformation radius and the Rhines scale, with a critical latitude near 30°N, where the deformation scale is similar to the Rhines scale.

[8] In this paper we reinterpret sea surface height (SSH) signals in the context of the aforementioned theoretical ideas. Specifically, we avoid the issue of jet formation, but posit that below a critical latitude baroclinic eddies transform some of their energy into Rossby waves, and that these waves dominate the surface height field. At higher latitudes, where Rossby wave frequencies are too small to be excited by the inverse cascade, the surface height field remains turbulent. We investigate this hypothesis as follows. Assuming quasi-geostrophic dynamics, we compute the local Rossby wave dispersion, but rather than make the long-wave approximation, we adjust the horizontal scale of first baroclinic waves to best fit the observed phase speeds, and thereby infer a length scale for the waves. In the tropics the fitted wavelength is close to both the Rhines scale and previously observed SSH scales. Outside the tropics, it is either impossible to match the observed phase speeds with Rossby wave speeds at any wavelength (probably because linear theory is inadequate) or the fitted wavelength lies near the deformation scale. Using surface drifter data to estimate the eddy timescale and energy level, we show that at high latitudes the turbulent timescale is faster than the Rossby wave timescale, so turbulence dominates, but at low latitudes the Rossby wave and turbulent timescales overlap, enabling the excitation of waves by turbulence.

[9] In section 2 we compare first baroclinic Rossby wave phase speeds calculated by G. Forget (Mapping observations in a dynamical framework: A 2004–2006 ocean atlas, submitted to *Journal of Physical Oceanography*, 2008; essentially, a mapping of Argo and satellite altimetric data using interpolation by the MITgcm) with observed altimetric phase speeds provided by C. Hughes (personal communication, 2006). Following on from *Chelton and Schlax* [1996] and *Killworth and Blundell* [2005] we include mean flow and stratification, and topographic slopes, but under quasi-geostrophic dynamics. We arrive at a conclusion consistent with *Chelton et al.* [2007]: in low to midlatitudes, phase speeds predicted by long-wave linear theory are typically faster than observed phase speeds. In section 3, where possible, we fit the phase speeds predicted by the linear model to observed phase speeds by adjusting the horizontal scale of the waves. We obtain a marked meridional variation in the scale of the fitted waves: equatorward of $\pm 30^\circ$ the fitted scale is large and gradually decreases with latitude, having an implied Rhines wavelength of about 600 km. Poleward of $\pm 30^\circ$ the linear fit begins to fail, and eventually fitted scales match the deformation scale. In section 4 we interpret our result via a comparison of turbulent and wave timescales. Finally, we estimate the critical latitude at which waves give

way to turbulence by making use of surface eddy velocities from drifter data, provided by N. Maximenko (personal communication, 2006). In section 5 we conclude.

2. Linear Rossby Waves

[10] Rossby waves result from the material conservation of potential vorticity (PV) in the presence of a mean gradient. As a parcel moves up or down the background mean PV gradient, its own PV must compensate, generating a restoring force toward the initial position. The result is a slow, large-scale westward propagating undulation of mean PV contours. Mean currents change the structure of the waves in two ways: by altering the background PV gradient (sometimes so much so that β is negligible), and by Doppler shifting the signal. A number of authors [Killworth *et al.*, 1997; Dewar and Morris, 2000; Killworth and Blundell, 2005; Maharaj *et al.*, 2007] have shown that the straightforward inclusion of the mean thermal wind currents in the linear Rossby wave problem leads to a much closer agreement between the observed phase speeds and theory. Here we take an approach closest to Killworth and Blundell [2007] [see also Smith, 2007] and compute phase speeds in the local quasi-geostrophic approximation, using the full background shear and stratification in a global hydrographic data set. Our focus, however, is on attempting to fit the linear results to the satellite data and thereby determining the limitations of linear wave theory when mean effects are fully included, and characterizing the scale of the waves that are consistent with the observed phase speeds. We now briefly outline the approach, relegating details to Appendix A.

[11] We assume, away from coasts, that Rossby wave and eddy dynamics are approximately local, and determined by the quasi-geostrophic equations, linearized about local vertical profiles of the mean velocity $\mathbf{U}(z) = U(z)\hat{x} + V(z)\hat{y}$ and squared buoyancy frequency $N^2(z) = -(g/\rho_0)d\bar{\rho}/dz$. Specifically, following Pedlosky [1984], we assume the mean velocity and stratification to be slowly varying functions of horizontal location. In other words, after using horizontal derivatives of the mean buoyancy field to compute the thermal wind velocities of the mean state, we consider the eddy and wave statistics over a box of, say, a few degrees in horizontal extent to be independent of horizontal position, except due to implicit slow changes in the local mean velocity and stratification. Importantly, in the local approximation, $\mathbf{U}(z)$ needs to be a solution to the quasi-geostrophic equation [Pedlosky, 1984].

[12] Denoting the slowly varying mean quantities with upper case letters, and the eddy perturbations with lower case, the linear QG potential vorticity equation is

$$\partial_t q + \mathbf{U} \cdot \nabla q + \mathbf{u} \cdot \nabla Q = 0, \quad -H < z < 0, \quad (1)$$

where $q = \nabla^2 \psi + (f^2/N^2)\psi_z$ is the eddy quasi-geostrophic potential vorticity (QGPV), ψ is the eddy stream function, $\mathbf{u} = -\psi_y\hat{x} + \psi_x\hat{y}$ is the eddy velocity, f is the local Coriolis parameter, and H is the local depth of the ocean. The mean QGPV gradient, determined from the mean velocity and stratification, is

$$\nabla Q = \left[\left(\frac{f^2}{N^2} V_z \right)_z \right] \hat{x} + \left[\beta - \left(\frac{f^2}{N^2} U_z \right)_z \right] \hat{y}. \quad (2)$$

Neglecting surface height deviations, the linearized upper boundary buoyancy equation is

$$\partial_t b + \mathbf{U} \cdot \nabla b + \mathbf{u} \cdot \nabla B = 0, \quad z = 0, \quad (3)$$

where the buoyancy anomaly is defined as $b = f\psi_z = -g\rho/\rho_0$, the mean buoyancy is $B = -g\bar{\rho}/\rho_0$, so the mean buoyancy gradient, via thermal wind balance, is $\nabla B = fV_z\hat{x} - fU_z\hat{y}$. Slowly varying bottom topography is included from the Smith and Sandwell [1997] global seafloor topography data set, using the approach of Smith [2007]. See Appendix A for details.

[13] Assuming a wave solution for the eddy components, $\psi(x, y, z, t) = \Re\{\hat{\psi}(z) \exp[i(kx + \ell y - \omega t)]\}$, and likewise for q and b , one obtains the linear eigenvalue problem,

$$(\mathbf{K} \cdot \mathbf{U} - \omega_n)\hat{b}_n = (\ell B_x - k B_y)\hat{\psi}_n, \quad z = 0, \quad (4a)$$

$$(\mathbf{K} \cdot \mathbf{U} - \omega_n)\hat{q}_n = (\ell Q_x - k Q_y)\hat{\psi}_n, \quad -H < z < 0, \quad (4b)$$

where $\mathbf{K} = (k, \ell)$, and $\hat{\psi}_n$ is the n th eigenvector, sometimes called a ‘‘vertical shear mode’’, and \hat{q}_n and \hat{b}_n are linear functions of $\hat{\psi}_n$. (The hat notation implies dependence on the wave number \mathbf{K} , which is suppressed for clarity.) The eigenvalues ω_n are the frequencies of the wave solutions, with the real part resulting in phase propagation and imaginary parts, if they exist, producing growth or decay of the wave. The problem is discretized in the vertical using a layered formulation; in the discretized case, there are as many shear modes as there are layers. The expressions for the discrete surface buoyancy \hat{b} and \hat{q} in terms of $\hat{\psi}$, and other details of the discretization can be found in Appendix A and are given by Smith [2007].

[14] Equations (4a) and (4b) are solved by first considering the neutral modes, which diagonalize the vertical derivatives in the stratification operator as follows. For a resting ocean ($\mathbf{U} = 0$, implying $B_x = B_y = Q_x = 0$ and $Q_y = \beta$), equations (4a) and (4b) reduce to the standard Rossby wave dispersion relation

$$\omega_m = \frac{-k\beta}{K^2 + K_m^2}, \quad (5)$$

where $K = |\mathbf{K}|$ and K_m is the m th deformation wave number, which is given by the following Sturm Liouville problem

$$\frac{d}{dz} \left(\frac{f^2}{N^2} \frac{d\Phi_m}{dz} \right) = -K_m^2 \Phi_m, \quad \frac{d\Phi_m}{dz} \Big|_{z=0, -H} = 0. \quad (6)$$

The eigenfunctions Φ_m are often called the ‘‘neutral modes’’; they form an orthonormal basis of the vertical structure in a resting ocean.

[15] The mean velocity and buoyancy fields are computed from Forget (submitted manuscript, 2008), as described in Appendix A, and these are used to construct the mean buoyancy and PV gradients. At each lateral position in the ocean, we then compute the neutral modes and their deformation scales from equation (6), as well as ω_n and $\hat{\psi}_n$ from the

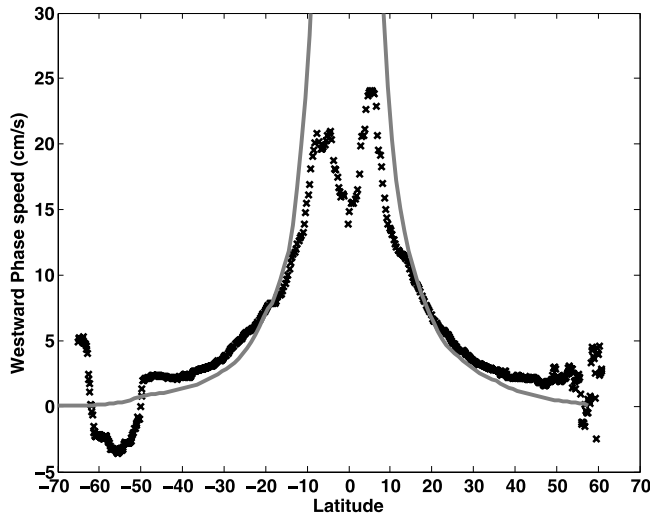


Figure 1. Westward phase speed estimated from Hughes’ data averaged from 170°W to 120°W (black crosses) plotted against the standard linear, first baroclinic, long Rossby wave phase speed (solid line) computed from Forget (submitted manuscript, 2008).

complete dispersion relations (4a) and (4b). We denote the zonal phase speed of this mode as

$$c_R = \frac{\omega_n}{k}.$$

2.1. Observations of Phase Propagation From Altimetry

[16] In the long-wave resting ocean limit the dominant first baroclinic mode has a westward phase speed given by equation (5) with $K = 0$, so $c_R = -\beta/K_1^2$. A zonal average of the long-wave phase speed is computed over the central Pacific (170°W to 120°W), and plotted against latitude in Figure 1. Also plotted are phase propagation observations provided by C. Hughes (personal communication, 2007), zonally averaged over the same range. Speeds at latitudes 20°S and 20°N are well captured by the classic long Rossby wave solution. However departures are observed at both low latitudes and high latitudes. Observed speeds reach a maximum near $\pm 5^\circ$. Poleward of 20° the Rossby wave solution diverges from the observations, reaching roughly a factor of two [Chelton and Schlax, 1996], and eastward propagation in the ACC region is also not captured. Figure 2 shows global maps of phase speed, “wavelikeness” and amplitude from Hughes’ data set. (The observed propagation speeds were calculated by Hughes from SSH observations in the following way. First, thin longitude (5 degrees) and tall time (11.5 years) strips are band-passed filtered in time from 5 to 57 weeks, then zonally averaged (at each time) and the annual and semiannual cycles are removed. A Radon transform was then performed by shifting each longitude such that signals traveling at a speed c line up horizontally, summing over longitude and taking the standard deviation in time. A wavelikeness parameter is also computed as the peak value of the Radon transform divided by its mean. On the basis of advice from Hughes we have filtered out observations with wavelikeness less than 1.5. Figure 2 shows global maps of the observed phase speed, wavelike-

ness (with white contour at 1.5), and the root mean square of the SSH amplitude.) Wavelikeness measures the precision of the distribution of phase speeds computed via the Radon transform at a given latitude, so one can already see from Figure 2 that low latitudes propagate mostly at coherent phase speeds while high latitudes exhibit a larger spread of propagation speeds, likely indicating a more turbulent flow.

[17] A global map of the deformation radii used to calculate the theoretical long-wave phase speeds in Figure 1 is shown in Figure 3, and was obtained using Forget (submitted manuscript, 2008). The vertical structure of the first baroclinic normal mode is plotted on the right for selected latitudes at 150°W in the Pacific Ocean, color-coded by the color of the crosses and using solid (dashed) lines in the Southern (Northern) Hemisphere respectively. The stratification tends to be more surface intensified at lower latitudes, where $\Phi_1(z=0)$ tends toward values near 4, and less surface intensified at high latitudes, where $\Phi_1(z=0)$ is between 2 and 3.

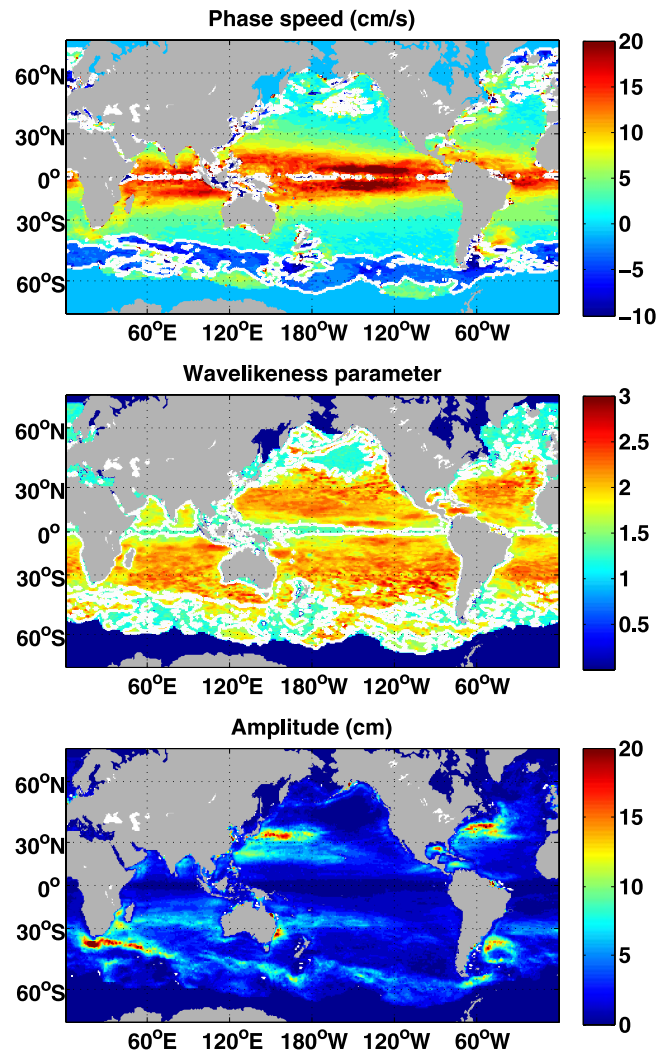


Figure 2. Hughes’ analysis of surface altimetric data. (top) Phase speed, with a white contour at 0, to differentiate westward and eastward propagating regions, (middle) wavelikeness (see text for details), with a contour at 1.5 to differentiate regions that are wavelike and not wavelike, and (bottom) a measure of amplitude.

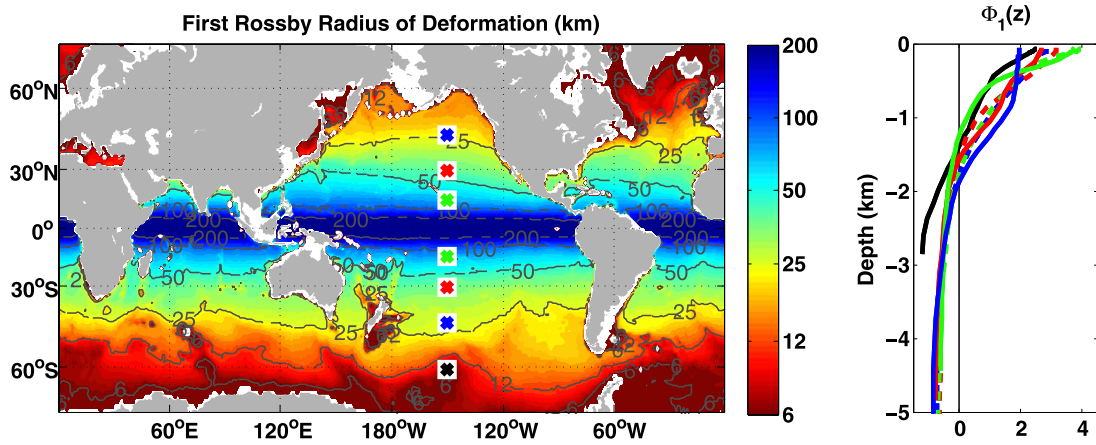


Figure 3. (left) Map of first internal deformation radius and (right) vertical structure of the first baroclinic mode, $\Phi_1(z)$, at the positions marked with colored crosses (at latitudes 60.5°S , 45.5°S , 30.5°S , 15.5°S , 14.5°N , 29.5°N , and 44.5°N , and longitude 150°W). The lines are color-coded with dashed lines indicating the Northern Hemisphere, and solid lines indicating the Southern Hemisphere.

Note that the color map saturates near the equator as deformation radii tend toward infinity.

2.2. Observations of Oceanic Currents and QGPV Gradients

[18] Figure 4 shows zonal averages of mean geostrophic zonal velocity and the meridional QGPV gradient Q_y from Forget (2008), with a black contour marking zero. Note that the QGPV gradient is nondimensionalized by the value of the planetary vorticity gradient at 30° , and that colors are saturated in the Q_y plot. The region above the dashed line indicates the layers from $z = 0$ to $z = -h$ that were averaged over in order to compute the upper PV sheet $f^2 U_z(z_0)/N^2$, as described in Appendix A. The important point to note is that ∇Q is clearly not well approximated by β . The salient features of the Q_y plot include (1) the zero crossing at 1 km depth in the ACC, just below the zonal jet which is responsible for significant baroclinically unstable growth and a steering level at depth, as reported by *Smith and Marshall* [2009], (2) the near-surface zero crossings at low latitudes may contain baroclinic Charney instabilities, (3) the western boundary currents near 40°N (and the zero crossings below them), and (4) the convectively unstable regions in high latitudes where bottom water formation occurs.

2.3. Applicability of Linear Theory

[19] We now consider the effects of including mean flow (U and ∇Q), estimated from Forget (2008), by using the dispersion relationship (4a) and (4b) then setting $K = 0$ (i.e., the long-wave approximation). For each location we choose the vertical shear mode $\hat{\psi}_n$ whose real part projects the most onto the first neutral mode $\Phi_1(z)$ after its mean is subtracted and it is normalized. Specifically, we choose $\hat{\psi}_n$ such that the following expression is maximized over n .

$$\max_n \int \Phi_1(\hat{\psi}_n - \overline{\hat{\psi}_n}) dz / \int (\hat{\psi}_n - \overline{\hat{\psi}_n})^2 dz.$$

The zonally averaged (from 170°W to 120°W) phase speeds are represented by the solid gray line in Figure 5. The observed central Pacific phase speeds from Figure 1 are also

replotted for comparison. The long-wave limit predicts speeds which are too fast in low latitudes and typically (but not always) too slow in high latitudes. It is pleasing, however, to now observe eastward propagation in the ACC, a consequence of downstream advection by the mean current.

[20] The assumed spatial scale of the waves also affects the predicted phase speeds. The same computation described above, but with deformation-scale waves ($\mathbf{K} = K_1 \hat{x}$), gives the dashed gray line in Figure 5. Assuming the deformation scale as a lower limit for the wavelength of the observed waves, the solid and dashed lines in Figure 5 bracket the range of values one can obtain for the phase speed from linear theory. We address this range of possibilities more fully in the next section.

3. Fitting Linear Model Phase Speeds to Observations

[21] Traditionally, the long-wave approximation has been used when interpreting altimetric signals in terms of Rossby wave theory. The influence of horizontal scale on Rossby wave speed has largely been neglected, except for calculations assuming uniform wavelengths of 500 km and 200 km reported by *Killworth and Blundell* [2005]. *Chelton et al.* [2007] argue that the propagation of the observed SSH variability is due to eddies rather than Rossby waves, and remark that, equatorward of 25° , eddy speeds are slower than the zonal phase speeds of nondispersive baroclinic Rossby waves predicted by the long-wave theory. Here we show, however, that such a difference in speed can be accounted for by linear Rossby waves when their wavelengths are chosen appropriately.

[22] Using equations (4a) and (4b) in its most general form, including bottom topography, Figure 6 shows both the best fit phase speeds (left) and the wavelengths associated with those phase speeds (right) for a zonal average from 170°W to 120°W in the Pacific (top) and a global zonal average (bottom). We have assumed that the fitted waves have an east–west orientation ($\ell = 0$). Setting $k = \ell$ makes little difference in the fitted wavelength, which is consistent with the finding by *Killworth and Blundell* [2005] of a weak

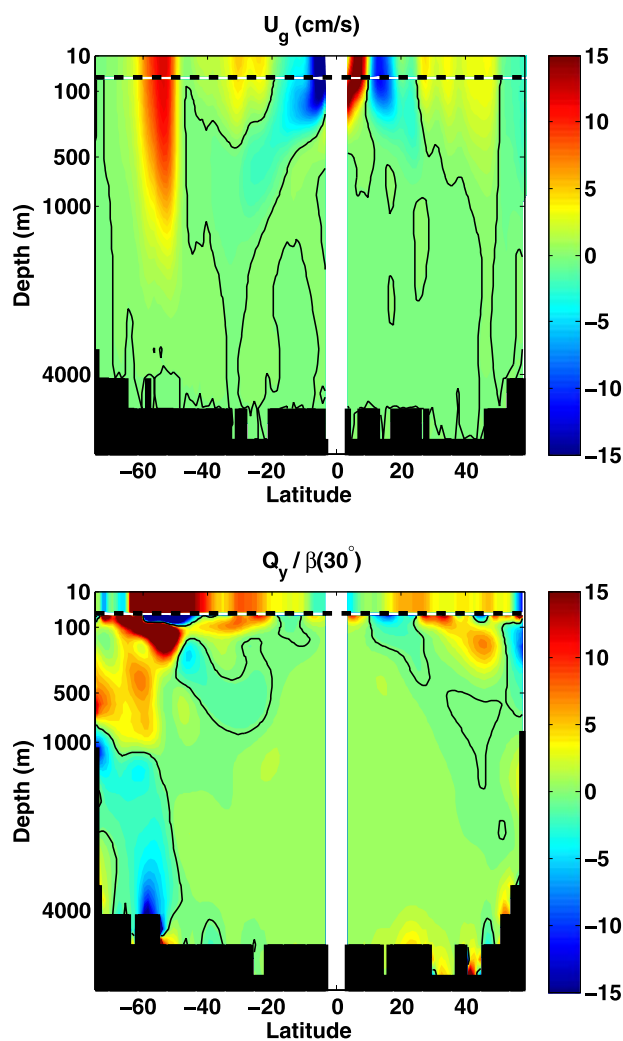


Figure 4. (top) Mean zonal velocity U , zonally averaged from 170°W to 120°W in the Pacific, and (bottom) meridional QGPV gradient zonally averaged over the same region. The PV gradient is normalized by the value of the planetary vorticity gradient, β , at 30 degrees. Note that the zero contour is indicated by black contours and that the color axis is saturated. The regions above the horizontal dashed line indicate the PV sheet layer.

dependence of phase velocity on orientation. In the fitted wavelengths plots, the black crosses correspond to individual latitudes, the solid gray curve is a smoother version of the black crosses, and the thin black line is the first deformation wavelength. (The fitted wavelengths are smoothed across latitudes using a 1-1-1 smoother defined by:

$$\lambda'_i = (\lambda_{i-1} + \lambda_i + \lambda_{i+1})/3,$$

where λ_i is the wavelength at latitude i and λ'_i is the smoothed value.) The fitted wavelengths typically lie between 600 km and 800 km in the tropics out to about 30° , with little or no dependence on the deformation wavelength. Note that the baroclinic Rhines scale (not shown) is roughly constant in the tropics, with a wavelength between 500 km and 700 km,

and diverges to infinity when the turbulent velocity surpasses the long-wave resting phase speed near $\pm 20^{\circ}$ (see below). However, poleward of $\pm 30^{\circ}$ it is more difficult to fit linear theory to the observations. There is a gap in fitted wavelength around $\pm 40^{\circ}$ where the linear theory fails to capture the observed phase speeds. At high latitudes, the best fit is obtained assuming scales near the deformation scale. The inability to fit the phase speeds at higher latitudes is suggestive that the “wave” signal is not linear in those regions. Clearly, though, the inclusion of wavelengths that result from a best fit of theoretical to observed phase speeds results in a greatly improved prediction.

[23] Figure 7 shows the importance of the planetary vorticity gradient β relative to the effect of mean flow U on the mean QGPV gradient ∇Q . Using the length scales computed by the best fit algorithm, we plot the phase speeds that result from setting $\beta = 0$ while keeping the observed U (thick dash-dotted line), as well as the phase speeds that result from setting $U = 0$ and $\nabla Q = \beta \hat{y}$ (thin dashed line). (The solid gray line and black crosses are the same as those plotted in Figure 6a.) The planetary gradient β is crucial in the tropics, while in the subtropics, U becomes increasingly important, particularly from 35°S to 20°S , where the mean shear accounts for much of the factor-of-two phase speed error discussed by *Chelton and Schlax* [1996]. At high latitudes the Doppler shift caused by U is crucial in capturing the downstream propagation in the ACC. Also note that the most unstable baroclinic modes have horizontal scales (not shown) of order of the deformation scale poleward of about 40° and do not increase toward the equator. Similarly the maximum baroclinic growth rates, and growth rates at our inferred scales, are significantly larger at high latitudes than low latitudes. See *Smith* [2007] for details of the linear instabilities. Figure 7 also shows the effect of bottom topography on phase speed. *Killworth and Blundell* [2003] and *Maharaj et al.* [2007] showed that topography is only important in the presence of a mean flow. Here the best fit phase speeds with mean flow and a flat bottom (thin black line) are compared

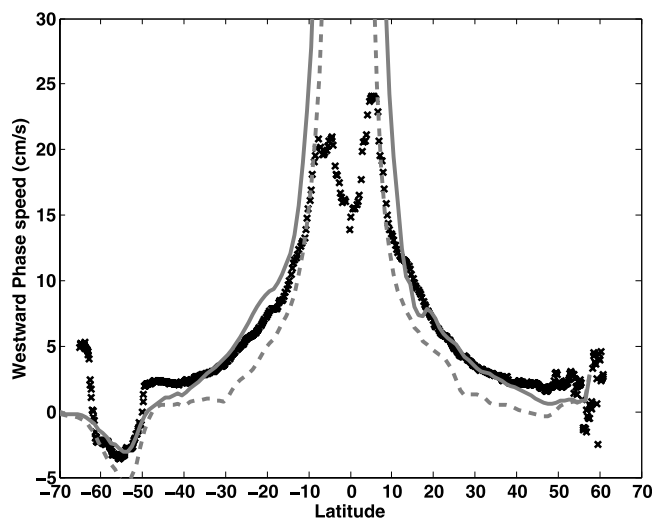


Figure 5. Hughes’ phase speed observations (black crosses) compared to linear theory in the presence of a mean current: long waves (gray solid line) and deformation scale waves (gray dashed line).

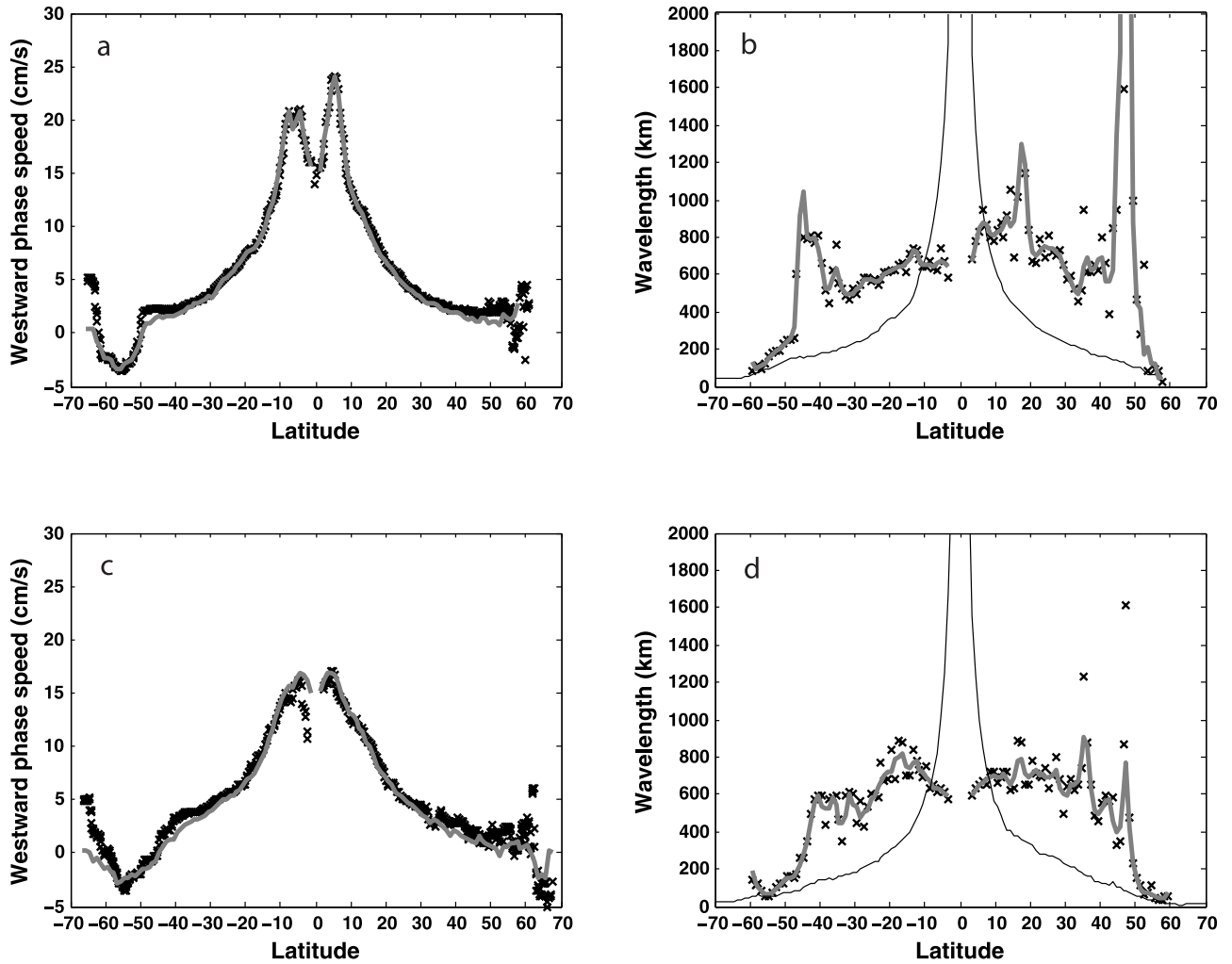


Figure 6. (a) Phase speeds according to linear theory (solid gray line) adjusted to give the best match to Hughes' data (black crosses). The fit is done for a zonal average over 170°W to 120°W in the Pacific. (b) Fitted wavelengths at each latitude (black crosses, gray line is a smoothed version) along with the deformation scale (thin solid line). (c) and (d) As in the top panels but zonally averaged across all oceans.

with the best fit speeds with topography (thick gray line). The fit is slightly better from 40° to 50° but the addition of topography is still not enough to completely fit the observations.

4. Wavelike and Turbulent Regimes in the Ocean

[24] A plausible interpretation of the results presented in Section 3 is that in low latitudes, baroclinic eddies give their energy to linear Rossby waves, whereas at high latitudes, Rossby waves are less easily generated, and the SSH field remains dominated by eddies. This can be understood in terms of a matching, or not, of turbulent and wave timescales, as discussed in the barotropic context by *Rhines* [1975] and *Vallis and Maltrud* [1993], and in a (first-mode) baroclinic context applied to the gas planets by *Theiss* [2004], *Smith* [2004], and *Theiss* [2006]. The central idea of the Rhines effect is that, as eddies grow in the inverse cascade, their timescale slows, and when this timescale matches the frequency of Rossby waves with the same spatial scale, turbulent energy may be converted into waves, and the cascade will slow tremendously. When this idea is applied to a puta-

tive interaction with baroclinic Rossby waves, there is the added complication that frequencies tend toward 0 at large scale (see Figure 8). In this case, only sufficiently weak eddies have timescales, at any wavelength, that intersect the Rossby wave dispersion curve.

[25] For illustrative purposes, one can estimate the wave number at which the intersection occurs by assuming a turbulent dispersion relationship of the form $\omega_t = ku_t$, where u_t is the turbulent velocity scale (the square root of the appropriate eddy kinetic energy). Setting this equal to the absolute value of the approximate Rossby wave frequency ($\omega_R \simeq -kQ_y / (K^2 + K_1^2)$) assuming that Q_x is small and U is either small or constant in z), we have (dividing by k)

$$u_t \sim \frac{Q_y}{K_1^2 + K^2}. \quad (7)$$

Solving for K gives the relationship $K^2 = Q_y/u_t - K_1^2$, for which there is a real solution only if $Q_y/u_t > K_1^2$. At fixed Q_y and K_1 , the implication is that waves can be generated (and the cascade inhibited) only when the turbulent energy is suf-

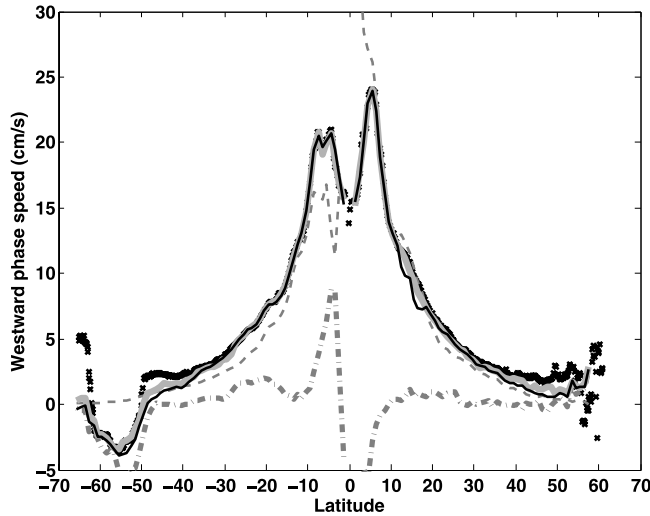


Figure 7. Comparison of the effects of β , mean currents, and topography. The crosses and thick gray solid line are identical to those in Figure 6a (zonal average over the Pacific region 170°W to 120°W). The thin black line shows the best fit phase speed with nonzero U and β but no topography, the thin dashed line corresponds to nonzero β , $U = 0$ and no topography, and the thick dash-dotted line corresponds to nonzero U , $\beta = 0$, and no topography. In all cases the best fit horizontal scale of Figure 6 is used.

ficiently small. On the other hand, assuming a constant u_t , and noting that Q_y (through its dependence on β) and K_1 (which is proportional to f) are dependent on latitude, the relationship (7) implies the existence of a critical latitude, poleward of which no intersection is possible.

[26] Let us now see what the data suggests about a relationship like (7). We replace the approximate Rossby wave dispersion relation with the frequencies from (4a) and (4b), using the fitted Rossby wave scales described in the previous section. The idea is illustrated in Figure 8, which shows zonally averaged Rossby wave frequency curves $\omega_R(k)$, plotted against zonal wavelength, at three latitudes in the tropical Pacific Ocean. Two hypothetical eddy frequency curves $\omega_t = ku_t$ (dashed lines) are added for comparison, with $u_t = 10 \text{ cm s}^{-1}$ and $u_t = 5 \text{ cm s}^{-1}$. At 10°S the eddy frequency curves intersect the Rossby wave frequencies at relatively small wavelengths, indicating that observed SSH length scales are certainly in the wave region. On the other hand, at 30°S even the 5 cm s⁻¹ curve fails to intersect $\omega_R(k)$. We thus expect little wavelike activity outside the tropics.

[27] We can improve the frequency comparison test further by using observations of surface drifter speeds to obtain estimates of u_t . A global map of the root mean square (rms) of the surface drifter data

$$u_{\text{rms}}(0) = \sqrt{|u'_{\text{drifter}}(z=0)|^2}$$

(courtesy of N. Maximenko) is shown in Figure 9, with its zonal average over 170°W to 120°W (the region within the rectangle) plotted in Figure 9 (right). The zonal average is strongly peaked at the equator, and more constant at extratropical latitudes. However, this may not be indicative of the distribution of total eddy kinetic energy, since the surface

velocity gives no information about the vertical structure of eddy motion. Additional assumptions are necessary to extract the relevant eddy velocity scale.

[28] Wunsch [1997] showed that, away from the equator, eddy velocities are primarily first baroclinic, with a smaller projection onto the barotropic mode, while nearer the equator, motions tend to have a more complex vertical structure, projecting onto many higher modes, approaching equipartition. Expanding $u_{\text{rms}}(z)$ in the neutral modes (6), we have

$$u_{\text{rms}}(z) = \sqrt{\left(\sum_{m=0}^{N_z} \Phi_m(z) u_m\right)^2 + \left(\sum_{m=0}^{N_z} \Phi_m(z) v_m\right)^2}$$

Following Wunsch [1997], we extract the vertical structure at each location by assuming that the rms velocity projects entirely onto the first baroclinic mode, which gives $|u_1| = u_{\text{rms}}(0)/|\Phi_1(0)|$. Since we are considering first baroclinic Rossby waves, the projection u_1 is the relevant eddy velocity scale, which is also the root vertical mean square velocity (if the flow is entirely first baroclinic), thus

$$u_t = \left[\frac{1}{H} \int_{-H}^0 u_{\text{rms}}(z)^2 dz\right]^{1/2} = u_{\text{rms}}(0)/\Phi_1(0)$$

where we have used the orthonormality of the neutral modes. (Suppose, instead of assuming that all the energy was in the first baroclinic mode, we imagined that $U(z)$ projected equally onto the barotropic and first baroclinic mode. Then

$$\begin{aligned} u_t &= \left[\frac{1}{H} \int u_{\text{rms}}(z)^2 dz\right]^{1/2} \\ &= \frac{u_{\text{rms}}(0)}{1 + \Phi_1(0)} \left[\frac{1}{H} \int (1 + \Phi_1(z))^2 dz\right]^{1/2} \\ &= \frac{\sqrt{2} u_{\text{rms}}(0)}{1 + \Phi_1(0)}, \end{aligned}$$

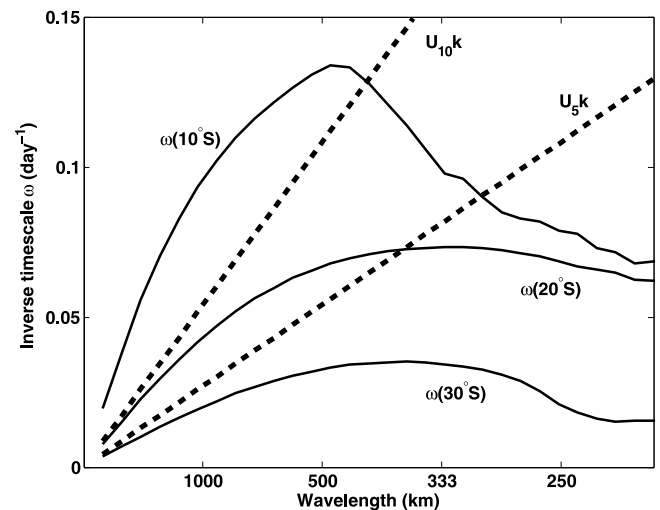


Figure 8. Dispersion relations for fitted phase speeds as a function of zonal wavelength (with meridional wave number $\ell = 0$) for latitudes in the South Pacific (10°S, 20°S and 30°S), compared with $\omega_t = ku_t$ with two values of u_t : 5 and 10 cm s⁻¹ (dashed lines).

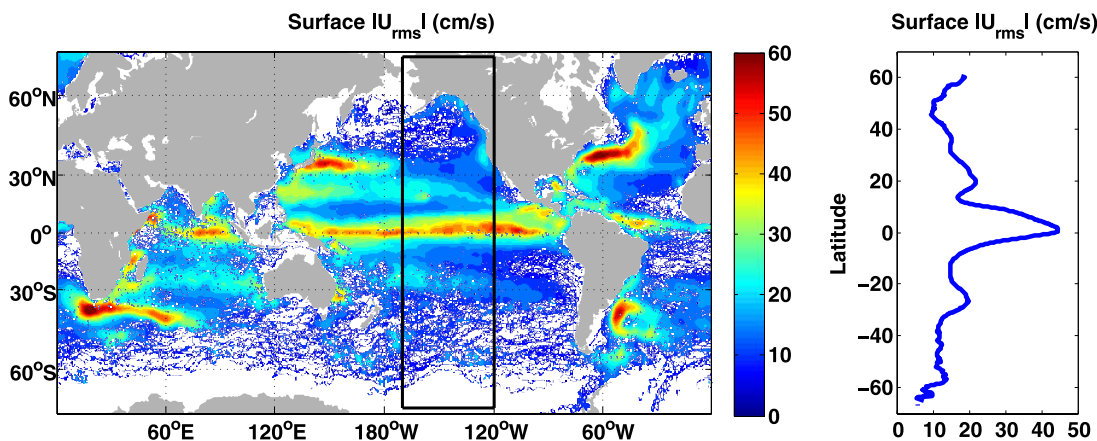


Figure 9. Root mean square eddy surface velocities (left) from *Maximenko et al.*'s [2005] drifter data and (right) zonal average thereof.

since the modes are orthonormal. In the world ocean $2 \leq \Phi_1(0) \leq 4$, so the ratio of this projected value to one which is entirely first baroclinic, as assumed in the text, is $0.94 \leq \sqrt{2}\Phi_1(0)/[1 + \Phi_1(0)] \leq 1.13$. An assumption of equipartition among N_z vertical modes unambiguously reduces u_t , roughly by a factor of roughly $\sqrt{N_z}$. The scaling by the first baroclinic mode has the effect of reducing the estimated turbulent velocity scale in regions of strongly surface intensified stratification, such as near the equator. In these regions, the first baroclinic mode itself is quite surface intensified, so $\Phi_1(0)$ can be considerably larger than one (see the modal structure in Figure 3). Physically, if the first neutral mode, onto which all the motion is assumed to project, is very surface intensified, then eddy velocities are weak at depth, so the total turbulent velocity estimate is diminished.

[29] Figure 10 shows the eddy velocity scale u_t and zonal Rossby phase speed c_R zonally averaged over 170°W to 120°W and plotted against latitude. These are essentially the left hand and equivalent right hand sides of equation (7). Our Figure 10 is similar to *Theiss* [2006, Figure 3] for Jupiter, except that here our dispersion relation is computed from the full vertical structure of the mean flow, rather than just the first baroclinic component (because of the dominance of the first baroclinic mode, however, the first baroclinic calculation is rather similar; not shown). Note that u_t is nearly constant with latitude, varying between and 5 and 10 cm s^{-1} ; the strong equatorial values have been reduced, through projection onto the surface-intensified first baroclinic mode, as explained above (if one assumed equipartition, the velocity estimate in the equatorial region would be reduced even further). In contrast, the (Doppler-shifted) Rossby wave speed varies markedly, exceeding 20 cm s^{-1} in the tropics and falling toward zero at higher latitudes (and even becoming prograde in the ACC). The crossover between the two curves occurs at a latitude of roughly $\pm 25^\circ$. Note that since we have assumed that the turbulent velocity scale u_t is entirely in the first baroclinic mode, the crossover latitudes should be considered as lower bounds.

[30] Figure 10 (bottom) shows the ratio of linear phase speeds c_R to the eddy velocity scale u_t , with dashed lines denoting $c_R/u_t = 2$ and $1/2$. *Theiss* [2006] shows that stormy regions on Jupiter are highly correlated with regions where

this ratio is less than one. Notably, $\pm 25^\circ$ is also the crossover latitude between linear wavelike behavior and nonlinear eddies found by *Chelton et al.* [2007]. Outside this latitude band, first-baroclinic Rossby wave timescales cannot match the turbulent timescales implied by u_t . Note that this would not preclude the formation of the midlatitude zonal jets observed by *Maximenko et al.* [2005] and *Richards et al.* [2006]: since barotropic Rossby waves are possible, turbulent energy can still accumulate around the dumbbell of *Vallis and Maltrud* [1993].

[31] Finally we return to a consideration of the spatial scales obtained by fitting linear Rossby wave theory to observed phase speeds, as in Figure 6. A global zonal average of the fitted wavelengths is plotted against latitude in Figure 11. Also plotted are both observed (black circles) and simulated

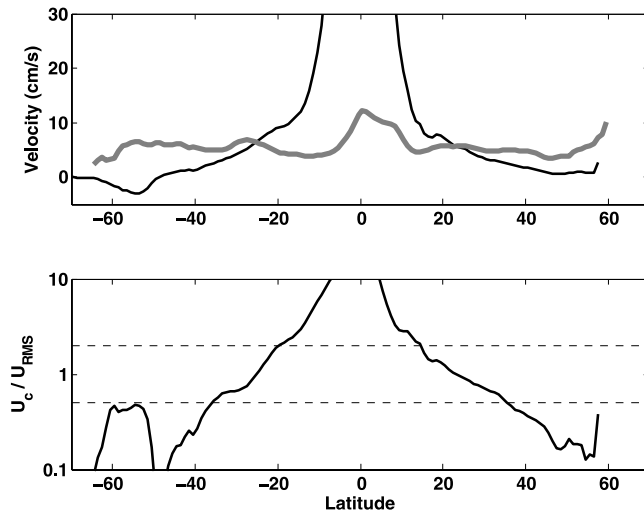


Figure 10. (top) Doppler shifted long-wave phase speed (thin black line) versus the root mean square of the eddy velocity u_t (thick gray line) from *Maximenko et al.*'s [2005] drifter data. It has been assumed that the eddy velocity is entirely in the first baroclinic mode. (bottom) The ratio c_R/u_t with dashed curves at ratios $1/2$ and 2 .

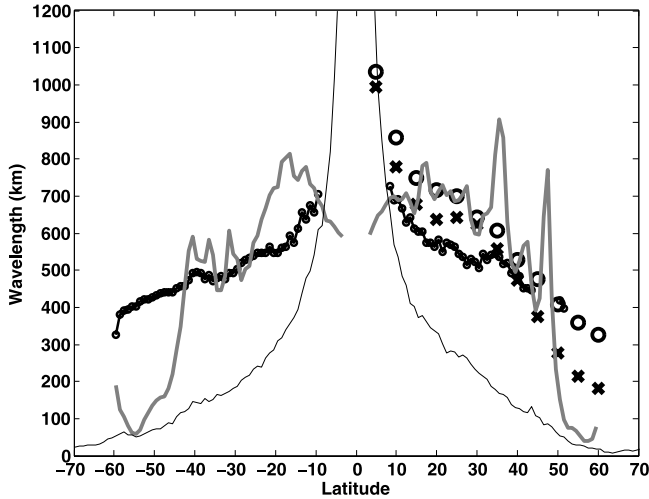


Figure 11. Comparison of fitted wavelengths over the global ocean (gray curve, taken from Figure 6d) against *Eden*'s [2007] observed (black circles) and simulated (black crosses) North Atlantic wavelengths (2π times the values given by *Eden* [2007, Figure 7a]), *Chelton et al.*'s [2007] globally observed wavelengths (π times eddy diameter, small black circles with solid line), and the deformation wavelength (thin black line). The Rhines wavelength, defined here as $\lambda_R = 2\pi(2u_t/\beta)^{1/2}$, where u_t is taken from Figure 10, is of order 600 km.

(black crosses) eddy wavelengths in the North Atlantic from *Eden* [2007], as well as globally observed wavelengths (small circles with line) from *Chelton et al.* [2007]. (*Chelton* provides eddy diameters, and here these are multiplied by π to give wavelengths.) The deformation wavelength (thin black line) is also plotted for reference. Note that the baroclinic Rhines wavelength (not shown) is also of the order of 600–700 km in the low latitudes, but diverges to infinity near $\pm 25^\circ$ where $c_R = u_t$ in Figure 10, so there is no baroclinic Rhines scale outside of this latitude band. At low latitudes all of the scales are in close agreement, while the fitted wavelength diverges from the observed eddy scales at latitudes poleward of about $\pm 40^\circ$. This is also near the latitude where *Eden*'s scales transition from a flatter Rhines scaling to a steeper deformation scaling. In the Southern Ocean there is a transition from westward propagation to eastward propagation upon entering the ACC region. Finally we note that, in contrast to *Eden* [2007], *Chelton*'s data do not exhibit a clear transitional latitude between Rhines scaling and deformation scaling. The reasons for this remain unclear.

5. Conclusions

[32] We have revisited the interpretation of altimetric phase speed signals in terms of linear Rossby wave theory. Given observations of the interior U and ∇Q fields (courtesy of Forget (submitted manuscript, 2008)), and assuming quasi-geostrophic theory, we adjusted the lateral scale of linear waves to best fit altimetric observations of westward phase propagation. We find that the implied scales have a well-defined meridional structure. In low latitudes the waves have a scale of 600 km or so, broadly consistent with an appro-

priately defined Rhines scale. In high latitudes it is more difficult to fit linear theory to the observations, but our attempts to do so imply a scale that is much smaller than in the tropics, closer to the local Rossby deformation scale. There is a rather abrupt transition from low-latitude to high-latitude scaling at $\pm 30^\circ$. These results are broadly consistent with observed and modeled eddy scales, as reported by *Eden* [2007].

[33] We put forward an interpretation of the reported results in terms of the interaction between turbulence and waves. Over vast regions of the ocean, at scales on or close to the Rossby deformation scale, baroclinic instability converts available potential energy to kinetic energy of turbulent geostrophic motion. Nonlinear interactions result in an up-scale energy transfer. At low latitudes, where we observe that $u_t < |c_R|$, turbulent energy cascades upscale from below readily excites Rossby waves. At higher latitudes, where $u_t > |c_R|$, turbulence cannot readily excite waves because of the weak overlap in timescales between turbulence and waves. Making use of surface drifter observations, we estimate that the latitude at which waves give way to turbulence coincides with that at which $u_t \sim |c_R|$, and is found to be $\pm 30^\circ$ or so, roughly consistent with the transition from waves to nonlinear eddies recently highlighted by *Chelton et al.* [2007].

Appendix A: Discretization of Linear Problem

[34] Forget (submitted manuscript, 2008) contains up to 50 layers (of thicknesses Δ_j) of potential temperature and salinity data at each (latitude, longitude) coordinate. We first compute annually averaged global potential temperature and salinity fields, and from these compute a neutral density field $\bar{\rho}$ using locally referenced pressure. Thermal wind balance is then used to compute the mean velocity field U , assuming a level of no motion at the bottom of the ocean [see *Smith*, 2007, appendix]. We define the top 5 layers, which are each 10 m thick, as a mixed layer of depth $h \equiv 50$ m. The mean buoyancy gradients $\nabla B = -(g/\rho_0)\nabla\bar{\rho}$ at the surface are averaged over the defined mixed layer, and then related to vertical shears via thermal wind

$$U_z(z_0) = -\frac{1}{fh} \int_{-h}^0 B_y dz, \quad V_z(z_0) = \frac{1}{fh} \int_{-h}^0 B_x dz.$$

The surface velocities themselves are obtained by averaging the velocities from the ocean atlas over h , viz.

$$U(z_0) = \frac{1}{h} \int_{-h}^0 U dz, \quad V(z_0) = \frac{1}{h} \int_{-h}^0 V dz. \quad (\text{A1})$$

[35] The linear problem is discretized, at each lateral location, onto the N_z discrete depths z_j of the data computed from Forget (submitted manuscript, 2008). The discrete surface buoyancy is given by

$$\hat{b}_m(z_0) = f \frac{\hat{q}_m(z_0) - \hat{q}_m(z_1)}{\Delta_0}.$$

and the discrete PV is

$$\hat{q}_m(z_j) = \frac{f^2}{\Delta_j} \left[\frac{\hat{\psi}_m(z_{j-1}) - \hat{\psi}_m(z_j)}{B(z_{j-1}) - B(z_j)} - \frac{\hat{\psi}_m(z_j) - \hat{\psi}_m(z_{j+1})}{B(z_j) - B(z_{j+1})} \right] - K^2 \hat{\psi}_m(z_j),$$

$$j = 1..N_z - 1.$$

The mean QGPV gradients $Q_x(z_j)$ and $Q_y(z_j)$ are given by equation (2), using the same vertical discretization, and simple horizontal finite differences to compute x and y derivatives. At the bottom, topography is added using the *Smith and Sandwell* [1997] global seafloor topography data set in the same way as *Smith* [2007]. At each latitude, longitude location in the calculation we linearly regress a best fit plane of the form $\eta(x, y) = \eta_0 + \alpha^x x + \alpha^y y$ using the surrounding $2^\circ \times 2^\circ$ section of topography. The slopes α^x and α^y are then added to the bottom (layer N) QGPV gradient as

$$\nabla Q^{\text{topo}} = \frac{f}{\Delta_N} (\alpha^x \hat{x} + \alpha^y \hat{y}).$$

The discrete version of (4a) and (4b) is then solved as a single matrix eigenvalue problem, using Matlab. As a simple test, solutions were compared with examples given by *Gill et al.* [1974].

[36] **Acknowledgments.** The authors thank Ryan Abernathy, Gael Forget, Chris Hughes, and Nikolai Maximenko for help with, and access to, data sets and Geoff Vallis for a helpful discussion on this subject.

References

- Arbic, B. K., and G. R. Flierl (2004), Baroclinically unstable geostrophic turbulence in the limits of strong and weak bottom Ekman friction: Application to midocean eddies, *J. Phys. Oceanogr.*, *34*, 2257–2273.
- Cessi, P., and F. Primeau (2001), Dissipative selection of low-frequency modes in a reduced gravity basin, *J. Phys. Oceanogr.*, *31*, 127–137.
- Chelton, D. B., and M. G. Schlax (1996), Global observations of oceanic Rossby waves, *Science*, *272*, 234–238.
- Chelton, D. B., M. G. Schlax, R. M. Samelson, and R. A. de Szoeke (2007), Global observations of westward energy propagation in the ocean: Rossby waves or nonlinear eddies?, *Geophys. Res. Lett.*, *34*, L15606, doi:10.1029/2007GL030812.
- Colin de Verdière, A., and R. Tailleux (2005), The interaction of a baroclinic mean flow with long Rossby waves, *J. Phys. Oceanogr.*, *35*, 865–879.
- Dewar, W. K. (1998), On “too fast” baroclinic planetary waves in the general circulation, *J. Phys. Oceanogr.*, *28*, 500–511.
- Dewar, W. K., and M. Y. Morris (2000), On the propagation of baroclinic waves in the general circulation, *J. Phys. Oceanogr.*, *30*, 2637–2649.
- Eden, C. (2007), Eddy length scales in the North Atlantic Ocean, *J. Geophys. Res.*, *112*, C06004, doi:10.1029/2006JC003901.
- Fu, L. L., and G. R. Flierl (1980), Nonlinear energy and enstrophy transfers in a realistically stratified ocean, *Dyn. Atmos. Oceans*, *4*, 219–246.
- Gill, A. E., J. S. A. Green, and A. J. Simmons (1974), Energy partition in the large-scale ocean circulation and the production of mid-ocean eddies, *Deep Sea Res.*, *21*, 499–528.
- Killworth, P. D., and J. R. Blundell (1999), The effect of bottom topography on the speed of long extratropical planetary waves, *J. Phys. Oceanogr.*, *29*, 2689–2710.
- Killworth, P. D., and J. R. Blundell (2003), Long extratropical planetary wave propagation in the presence of slowly varying mean flow and bottom topography. Part I: The local problem, *J. Phys. Oceanogr.*, *33*, 784–801.
- Killworth, P. D., and J. R. Blundell (2005), The dispersion relation of planetary waves in the presence of mean flow and topography. Part II: Two-dimensional examples and global results, *J. Phys. Oceanogr.*, *35*, 2110–2133.
- Killworth, P. D., and J. R. Blundell (2007), Planetary wave response to surface forcing and to instability in the presence of mean flow and topography, *J. Phys. Oceanogr.*, *37*, 1297–1320.
- Killworth, P. D., D. B. Chelton, and R. A. D. Szoeke (1997), The speed of observed and theoretical long extratropical planetary waves, *J. Phys. Oceanogr.*, *29*, 1946–1966.
- LaCasce, J. H., and J. Pedlosky (2004), The instability of Rossby basin modes and the oceanic eddy field, *J. Phys. Oceanogr.*, *34*, 2027–2041.
- Maharaj, A. M., P. Cipollini, N. J. Holbrook, P. D. Killworth, and J. R. Blundell (2007), An evaluation of the classical and extended Rossby wave theories in explaining spectral estimates of the first few baroclinic modes in the South Pacific Ocean, *Ocean Dyn.*, *57*, 173–187.
- Maximenko, N. A., B. Bang, and H. Sasaki (2005), Observational evidence of alternative zonal jets in the world ocean, *Geophys. Res. Lett.*, *32*, L12607, doi:10.1029/2005GL022728.
- Pedlosky, J. (1984), The equations for geostrophic motion in the ocean, *J. Phys. Oceanogr.*, *14*, 448–455.
- Rhines, P. B. (1975), Waves and turbulence on a β -plane, *J. Fluid. Mech.*, *69*, 417–443.
- Richards, K. J., N. A. Maximenko, F. O. Bryan, and H. Sasaki (2006), Zonal jets in the Pacific Ocean, *Geophys. Res. Lett.*, *33*, L03605, doi:10.1029/2005GL024645.
- Schlösser, F., and C. Eden (2007), Diagnosing the energy cascade in a model of the North Atlantic, *Geophys. Res. Lett.*, *34*, L02604, doi:10.1029/2006GL027813.
- Scott, R. B., and B. K. Arbic (2007), Spectral energy fluxes in geostrophic turbulence: Implications for ocean energetics, *J. Phys. Oceanogr.*, *37*, 673–688.
- Scott, R. B., and F. Wang (2005), Direct evidence of an oceanic inverse kinetic energy cascade from satellite altimetry, *J. Phys. Oceanogr.*, *35*, 1650–1666.
- Scott, R. K., and L. M. Polvani (2007), Forced-dissipative shallow-water turbulence on the sphere and the atmospheric circulation of the giant planets, *J. Atmos. Sci.*, *64*, 3158–3176.
- Smith, K. S. (2004), A local model for planetary atmospheres forced by small-scale convection, *J. Atmos. Sci.*, *61*, 1420–1433.
- Smith, K. S. (2007), The geography of linear baroclinic instability in Earth’s oceans, *J. Mar. Res.*, *65*, 655–683.
- Smith, K. S., and J. Marshall (2009), Evidence for enhanced eddy mixing at mid-depth in the Southern Ocean, *J. Phys. Oceanogr.*, in press.
- Smith, K. S., and G. K. Vallis (2001), The scales and equilibration of mid-ocean eddies: Freely evolving flow, *J. Phys. Oceanogr.*, *31*, 554–571.
- Smith, W. H. F., and D. T. Sandwell (1997), Global seafloor topography from satellite altimetry and ship depth soundings, *Science*, *277*, 1957–1962.
- Stammer, D. (1997), Global characteristics of ocean variability estimated from regional TOPEX/POSEIDON altimeter measurements, *J. Phys. Oceanogr.*, *27*, 1743–1769.
- Theiss, J. (2004), Equatorward energy cascade, critical latitude, and the predominance of cyclonic vortices in geostrophic turbulence, *J. Phys. Oceanogr.*, *34*, 1663–1678.
- Theiss, J. (2006), A generalized Rhines effect on storms on Jupiter, *Geophys. Res. Lett.*, *33*, L08809, doi:10.1029/2005GL025379.
- Thompson, A. F., and W. R. Young (2006), Scaling baroclinic eddy fluxes: Vortices and energy balance, *J. Phys. Oceanogr.*, *36*, 720–738.
- Vallis, G. K., and M. E. Maltrud (1993), Generation of mean flows and jets on a beta plane and over topography, *J. Phys. Oceanogr.*, *23*, 1346–1362.
- Wunsch, C. (1997), The vertical partition of oceanic horizontal kinetic energy, *J. Phys. Oceanogr.*, *27*, 1770–1794.

J. Marshall, Department of Earth, Atmospheric and Planetary Sciences, Massachusetts Institute of Technology, 77 Massachusetts Avenue, Cambridge, MA 02139, USA. (jmarsh@mit.edu)

K. S. Smith and R. Tulloch, Center for Atmosphere Ocean Science, Courant Institute, New York University, 251 Mercer Street, New York, NY 10012, USA. (shafer@cims.nyu.edu; tulloch@cims.nyu.edu)